High Power Laser Science and Engineering, (2025), Vol. 13, e64, 9 pages.
doi:10.1017/hpl.2025.10036

HIGH POWER LASER SCIENCE AND ENGINEERING

RESEARCH ARTICLE

Pulse-length dependence of the laser-induced damage behavior of a fused-silica antireflective metasurface

Kyle R. P. Kafka, Brittany Hoffman, Hu Huang, Alexei Kozlov, Marek Stehlik, and Stavros G. Demos

Laboratory for Laser Energetics, University of Rochester, Rochester, NY, USA

(Received 8 March 2025; revised 16 April 2025; accepted 15 May 2025)

Abstract

A broadband, antireflective metasurface optic on a silica substrate is subjected to laser-induced damage-threshold measurements to quantify its performance under exposure to high-intensity/fluence laser pulses in the near-infrared at four pulse durations, ranging from 20 fs to 1.4 ns. The performance of the metasurface is benchmarked against that obtained from an equivalent bare fused-silica substrate that did not receive reactive-ion-etching metasurface treatment. Results showed that the damage threshold of the antireflective metasurface was always lower than the input-surface damage threshold of the untreated substrate. The damage initiations with nanosecond and picosecond pulses resulted in localized modification and removal of the nanostructures, whereas the onset of laser-induced modification with 20-fs pulses in a vacuum environment manifested as changes in the optical and electronic properties without significant material removal. The broader goal of this work is to develop a preliminary understanding of the laser-induced failure mechanisms of silica-based metasurface optics.

Keywords: antireflection; fused silica; laser-induced damage; metasurface

1. Introduction

Photonic metasurfaces are nanostructured surfaces comprising elements that are subwavelength in size that enable control of the amplitude, phase, and polarization of incident light. Although the structure of metasurfaces can be tailored to achieve a multitude of different optical functions[1,2], the majority of current-generation devices are not suitable for high-peak-power laser applications, primarily due to optical losses introduced by the structures. The losses typically originate from the chosen high-refractive-index materials (metals, semiconductors or small-band-gap dielectrics) that are known to exhibit low tolerance in handling the laser power (e.g., low laser-induced-damage threshold (LIDT)). To overcome this issue, metasurfaces must contain large-band-gap dielectric materials and minimize electric-field enhancement within the structured surface material. Example demonstrations of metasurface optics composed of laser-damage-resistant materials include antireflective metasurfaces[3,4] and birefringent metasurface waveplates[5].

Antireflective metasurfaces have been shown to be manufacturable using high-damage-threshold materials such as fused silica. The relative volume fractions of the structures and the respective spaces between structures constitute an average refractive index (understood using an effective medium approximation) that varies with depth and leads to destructive interference of the reflected wave component, similar to an antireflection coating. The lateral size, shape and distribution of the structural elements impact the spectral performance. Fabrication of antireflective metasurfaces has been demonstrated using various methods, including etching patterns (e.g., 'moth-eye') with lithography[6,7] and printing patterns with nano-imprint lithography[8], as well as forming self-organized 'random' nanotextures by reactive ion etching[9–11] or direct laser processing[12,13]. Conventional antireflection approaches often involve thin-film coatings that usually cause a significant reduction in damage resistance[14] or involve sol–gel coatings that are known to be less environmentally stable. Although advances in lithographic technology have enabled the manufacture of patterned metasurfaces with increased control of feature size and shape, random-antireflective (RAR) nanotextures naturally achieve small feature sizes without the need for high-resolution lithography, which may offer benefits in scalability to larger-aperture optics. RAR metasurfaces formed by directly reactive-ion etching the surface of fused silica are commercially available and have been shown to achieve excellent antireflective and broad bandwidth performance[9,11].

Correspondence to: K. R. P. Kafka, Laboratory for Laser Energetics, University of Rochester, 250 East River Road, Rochester, NY 14623-1299, USA. Email: kkaf@lle.rochester.edu

The laser-induced damage performance of silica RAR metasurfaces has been reported previously for nanosecond pulse lasers[10,13], but not for picosecond or femtosecond durations. The nanosecond-duration literature results suggest the potential for comparable damage resistance to untreated substrates, although typically, the observed damage-threshold fluences of the metasurfaces were lower than those of high-quality non-textured substrates. Since the damage-initiation mechanisms are generally known to change as a function of pulse duration, particularly across the few-picosecond to femtosecond range[15], the nanosecond damage performance may not accurately represent the behavior at shorter pulses, as has been previously demonstrated for the case of thin films[16]. Although antireflective technologies see less use in short-pulse laser applications, owing to the reduced demand for transmissive optics, certain critical transmissive components often cannot be avoided, such as nonlinear crystals and vacuum windows.

In this work, we present a study aiming to understand the high-fluence response of fused-silica samples that employ RAR metasurfaces under exposure to near-infrared laser pulses with durations of 1.4 ns, 10 ps, 0.8 ps, and 20 fs, thus spanning about five orders of magnitude. The results demonstrate that the damage threshold of the metasurface was about 20%–40% of the value measured for the input surface of the untextured substrate. Finite-difference time-domain three-dimensional (3D) simulations indicated localized electric-field enhancement introduced by the nanostructures, which may be responsible, in part, for the reduction of damage resistance. Damage initiation with nanosecond and picosecond pulses caused localized melting and/or removal of nanostructure elements, whereas the onset of observable material modifications with 20-fs pulses in a vacuum environment manifested as changes in the optical and electronic properties of the near-surface material without significant material removal. We hypothesize that the results of this work are representative of more general behaviors inherent to metasurface optics.

2. Methods

The RAR metasurface samples used in this work were acquired commercially from TelAztec and are fabricated using reactive ion etching (without an etch mask)[9]. Commercially polished substrates of Corning 7980 fused silica were used for both the RAR metasurface and corresponding untextured samples. The metasurface sample was textured on both sides with the vendor catalog number 'RAR-L2', which is optimized for a reflection minimum near 1064 nm and provides significant antireflection from 0.4 to 1.1 μm. Example scanning electron microscopy (SEM) images of one of the metasurfaces are shown in Figure 1, indicating approximately 50-nm-diameter needle-like features. The as-observed structures in Figure 1 are somewhat distorted due to the use of platinum coating for SEM imaging.

Laser-induced damage testing was executed using three separate systems to accommodate the range of pulse durations from 1.4 ns to 20 fs, with the various test conditions summarized in Table 1. Implementation of the laser and damage-testing systems has been discussed previously, at the nanosecond[17], picosecond[18] and femtosecond[19] levels. Overall, various sites across each sample were subjected to a range of fluence levels, and the sample surface was monitored by an *in situ* dark-field microscope before and after irradiation to detect nonreversible material modifications (i.e., damage) induced by the laser. After the testing, an offline differential interference contrast (DIC) microscope

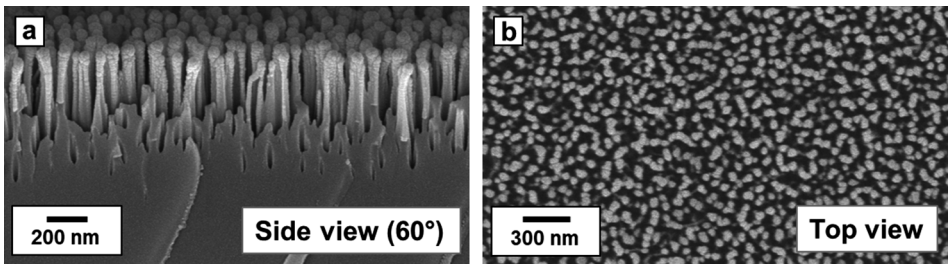

Figure 1. Scanning electron micrographs of the RAR metasurface without laser exposure, showing (a) side view at 60° from normal and (b) top view. Note that the bulbous appearance of the tips of the structures is an artifact of the platinum coating process required for imaging and that the actual features are more pointed.

Table 1. Summary of parameters used in the three laser-induced damage-testing systems.

System	Wavelength (nm)	Angle of incidence	Test ambience	Pulse duration	Test protocols
ns	1053	7°	Air	1.4 ns	1-on-1, R-on-1
ps	1053	1°	Vacuum	10 ps, 0.8 ps	1-on-1, R-on-1
fs	900	1°	Vacuum	20 fs	1-on-1, 100-on-1

https://doi.org/10.1017/hpl.2025.10036 Published online by Cambridge University Press

was used to confirm the results detected during the experiments. The beam size ranged from roughly 300 to 500 μm ($1/e^2$ diameter), depending on which laser system was used.

In the damage testing, any modification that is observable via optical microscopy examination is defined as 'damage', while the onset of observed damage among all sites within a test is defined as the LIDT for that set of test conditions. The test protocols involve single-pulse (1-on-1) and multipulse (R-on-1 or S-on-1) exposures to gauge different performance aspects. The 1-on-1 test protocol irradiates each site with a single pulse at a predetermined fluence, and the result of each site is assigned to 'damage' or 'no damage'. The R-on-1 protocol irradiates each site with multiple pulses where the laser fluence is ramped from low to high values until damage initiation is observed. This protocol is relevant for situations exhibiting laser conditioning (an improvement of the measured LIDT), where sample defects and/or contamination can be removed or passivated by lower-fluence pulses and effectively increase the damage resistance. The S-on-1 test ($S = 100$ here) is similar to 1-on-1, except that S pulses of the predetermined fluence irradiate each site (fluence varies among sites). This protocol is relevant for situations exhibiting laser fatigue (sometimes called 'incubation'), where the increased total dose of exposed pulses leads to a reduction of damage resistance.

In the experiments reported in this work, only the damage resistance of the front surface of the optics was measured in order to avoid conflation with an expected reduction of the LIDT at the exit surface of bare substrates due to electric-field intensification caused by the internal Fresnel reflection. Hence, the performance of the metasurface is effectively benchmarked against the unstructured material rather than against the usable fluence level of an uncoated optic, which has little practical value.

The morphology of the test sites was further analyzed using DIC microscopy and SEM. Further analysis in a subset of the cases involved atomic force microscopy (AFM), fluorescence microscopy, and/or functional characterization. The SEM analysis employed both an in-column backscattered-electron (BSE) detector and a secondary-electron (SE) detector, providing higher-resolution or topography-sensitive images, respectively. In this work, BSE-SEM images are the default type unless indicated. The fluorescence microscopy system used 260- or 360-nm laser excitation (incident obliquely), with a 400-nm longpass spectral filter in the imaging system to block scattered excitation light. The functional characterization involved transmission measurements of a focused beam aligned to propagate through the damage site under interrogation, performed after the damage testing. The transmission measurements were performed using a pair of energy or power meters to compare the incident and transmitted flux, and had a sensitivity limit of about 0.05%. The transmission was carried out with two sources: a (broadband) femtosecond laser (with significant attenuation) and repeated with a 1030-nm continuous-wave laser. Similar results were achieved with both sources.

3. Experimental results

This section will describe the investigation of observed damage morphologies, followed by a summary of the LIDT performance.

3.1. Morphology

An example of damage initiation formed under 1.4-ns pulse duration, 1-on-1 testing, is shown in Figure 2. This case, representing the near-LIDT observed morphology, contains only one damage site within the irradiated area. The diameter of these damage sites was always more than 10 μm (in this example, it is about 50 μm). The center of the damage site indicates a submicrometer (or smaller) damage-initiation (precursor) location that gives rise to the formation of an ablation crater. Within the ablation crater are (fiber-like) projections that may be formed by the ejection of liquefied glass, oriented radially and stretched by the pressure gradient generated during the ablation event (Figure 2(e)). Comparison of Figures 2(c) and 2(d) clearly shows that surrounding the ablation crater is a large region of modified nanostructures that appear to be associated with exposure to temperatures above the melting point.

Typical images of damage sites generated under exposure to the 10-ps, 1-on-1 protocol near the LIDT are shown in Figure 3, where tens of damage-initiation sites can be seen in the DIC microscope image in Figure 3(a) and SEM image in Figure 3(b) in which each has a diameter of approximately $\leq$1 μm. It must be noted that the small dark spots in the DIC images are an artifact and should be ignored. The SEM analysis reveals that there are two types of damage morphologies present. The larger type of damage morphology (Figure 3(c)) appears to be associated with the ablation of submicrometer sections of the nanostructure, surrounded by a region where the nanotexture elements have been fused together. This morphology corresponds to the onset of material modification detected by the *in situ* microscope system, owing to increased scattering. The SE-SEM image of Figure 3(b) (dashed region), however, indicates a second, more subtle damage mechanism that involves only the ablation of sections of a few adjacent nanostructure elements. In fact, these small, infrequent pits are nearly undetectable in BSE-SEM images, as shown in the center of Figure 3(d). Both of these morphologies were characterized using AFM with a high-aspect-ratio tip, and depths were measured to be about 250 and 100 nm for the larger and smaller morphologies, respectively.

https://doi.org/10.1017/hpl.2025.10036 Published online by Cambridge University Press

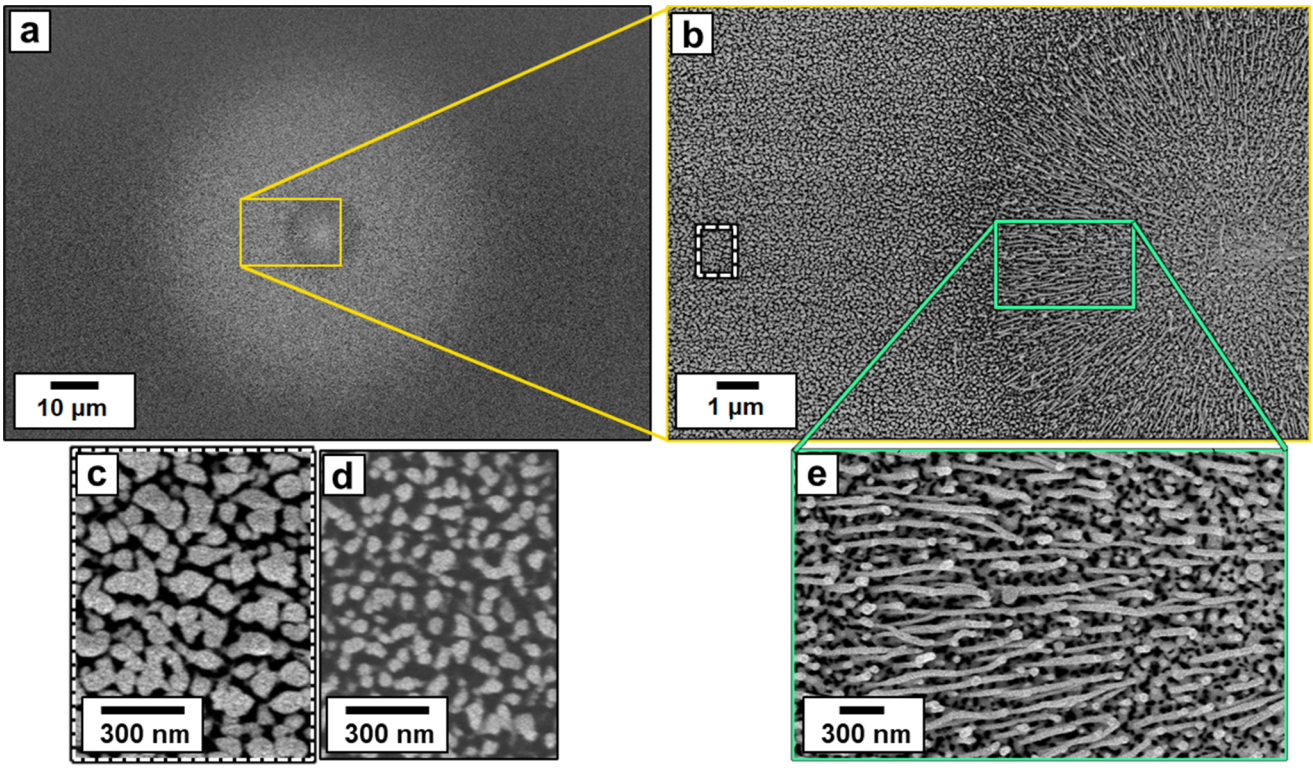

Figure 2. SEM images of an example site formed by 1.4-ns pulse duration, at 24 J/cm^2. (a) Overview of the entire damage site, (b) zoom-in as indicated in yellow, (c) further zoom-in as indicated in the white dashed region showing the modified nanostructure, as compared with (d) the pristine location on the same scale. (e) Further zoom-in, as indicated in green, showing elongated features in the crater.

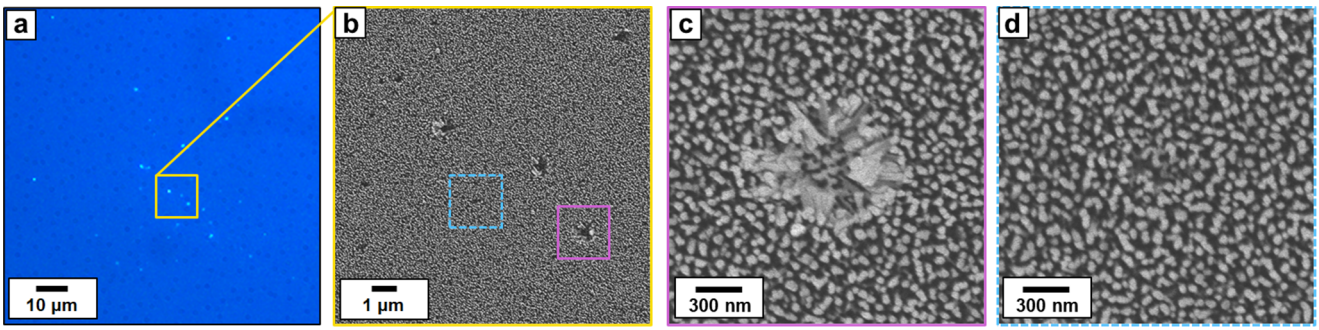

Figure 3. Images of a damage site formed by 10-ps pulse duration, at 2.6 J/cm^2. (a) DIC microscope image overview, (b) SE-SEM image of a region showing two types of damages, which are further magnified to show the (c) larger type in the solid-line region and (d) smaller type in the dashed line region. Both (c) and (d) are BSE-SEM images.

The second type of damage morphology observed under 10-ps exposure is the dominant damage morphology under exposure to 0.8-ps pulse duration, although the ablated nanopits are generated at a density that is more than an order of magnitude greater than at 10 ps. As can be seen in the 1-on-1 site DIC image of Figure 4(a), the damage appears like a fine speckle pattern of pits within the laser-irradiated area. The SE-SEM image in Figure 4(a) demonstrates that the damage density for this site is of the order of approximately 1 μm^{-2}, and some of the features can be identified in BSE-SEM images, as seen in Figure 4(c).

The damage morphology under 20-fs pulses was found to be distinctly different since no visible amount of ablation of material was observable until fluences significantly above the onset of material modification (defined as the LIDT). To more clearly detect and visualize the accumulation of these modifications, Figure 5 depicts an example 100-on-1 damage site. The *in situ* microscopy detected a modification associated with the bright areas, as shown in Figure 5(a), and a complementary modification seen in the surrounding dark region of the sample surface corresponding to areas exposed to lower fluence. Because the *in situ* microscopy images represent the ratio of the *in situ* dark-field microscope images before and after the train of 100 laser pulses, bright regions indicate an increased signal of scattered illumination light (provided by a 450-nm continuous-wave laser), while

https://doi.org/10.1017/hpl.2025.10036 Published online by Cambridge University Press

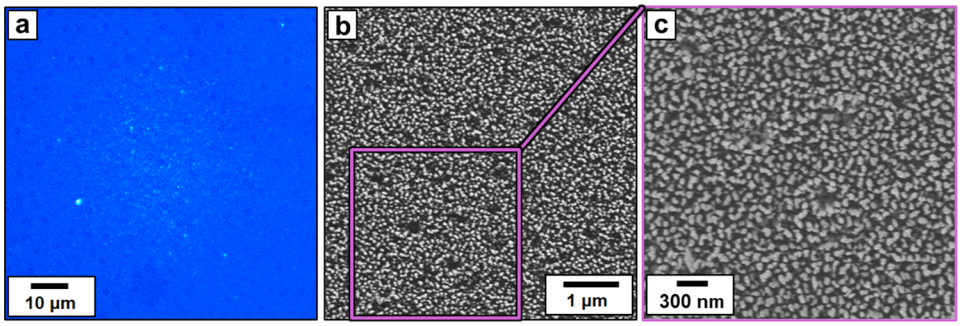

Figure 4. Images of a damage site formed by 0.8-ps pulse duration, at 2.4 J/cm^2. (a) DIC image overview, (b) SE-SEM image near the center of the site and (c) BSE-SEM image of the solid-line region, magnifying the shallow damage pits.

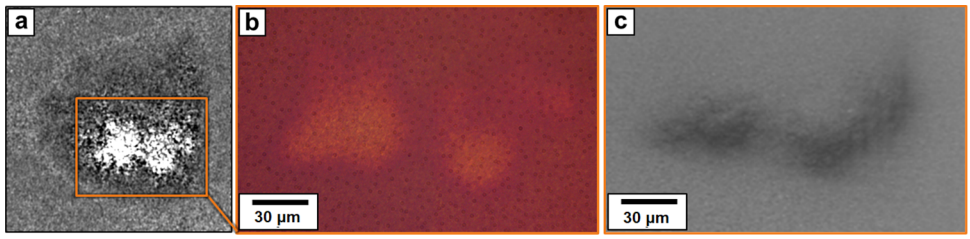

Figure 5. Images of a damage site formed by 100 pulses of 20-fs duration, at 1.1 J/cm^2, collected via (a) *in situ* dark-field microscopy, (b) DIC microscopy and (c) SEM. The rectangle in (a) corresponds to the imaged region of (b) and (c), indicating detected modifications not observed in DIC and SEM images.

the dark regions indicate the decreased signal of scattered illumination light.

The DIC image (Figure 5(b)) of the same site indicates a modification that is typically referred to as the 'color change' failure mode in the literature[20], which is associated with non-catastrophic but irreversible modification of dielectric materials in optics subjected to repeated exposures of femtosecond pulses. Figure 5(c) shows the same location on the same scale (low resolution), imaged with the SEM, which indicates surface 'charging' (dark region) in the area corresponding to the damage pattern observed with DIC microscopy (Figure 5(b)). Although this natively insulating sample was coated with platinum (after all damage testing was completed) to facilitate SEM imaging, this observed surface charging suggests the presence of a significant modification of the electronic structure (i.e., defects generated) within the laser-irradiated area.

Defect generation in silica has been shown to arise from exposure to various types of radiation, including ions and particles[21–25], ultraviolet laser pulses of nanosecond-scale duration[24,26] and near-infrared laser pulses of femtosecond-scale duration[27,28]. To investigate both of the laser-modified morphologies observed under 20-fs irradiation in more detail in consideration of this prior knowledge on defects in silica, 100-on-1 testing was repeated on additional RAR silica samples, and the exposed sites were imaged using fluorescence microscopy under 260- or 360-nm excitation to selectively and resonantly excite different defect populations. This analysis aimed to detect and image the correlation of the material changes observed under DIC and scanning electron microscopy with the defect species that may be formed on the affected areas of the surface.

Typical examples of corresponding fluorescence images as a function of fluence are shown in Figure 6. Under 260-nm excitation, the central region (exposed to higher fluence) exhibits stronger emission, while in the surrounding area (exposed to lower laser fluence), the emission is significantly reduced. In contrast, under 360-nm excitation, the outer (lower-fluence) region exhibits stronger emission, while the central region exhibits reduced emission. This behavior may be explained by considering the properties of the two dominant photoluminescent defect species that are generated in silica: (1) oxygen-deficient centers (ODCs) and (2) non-bridging oxygen hole centers (NBOHCs). Using 260-nm excitation, the emission cross-section of an ODC defect is known to be much higher compared to the NBOHC, while the opposite is the case under 360-nm excitation[26]. Therefore, the images shown in Figure 6 allow one to capture the relative localization of these two types of defects within the laser-modified region, where the lower-fluence morphology is primarily associated with NBOHC defects and the higher-fluence morphology with ODC defects.

To characterize the impact of these laser-generated defects on the functional performance of the RAR surface, transmission measurements were performed using a focused beam aligned to the respective femtosecond-laser-modified areas. The results showed that there was a transmission loss of about 0.4% in the areas exposed to higher fluence (ODC defects), which is consistent with the increased scattering observed for this type of damage in dark-field microscopy.

https://doi.org/10.1017/hpl.2025.10036 Published online by Cambridge University Press

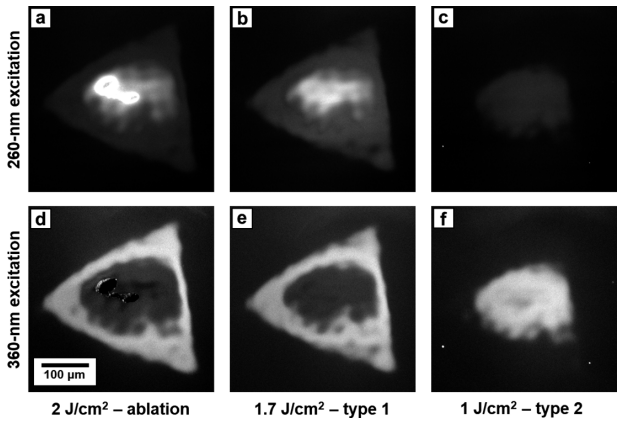

Figure 6. Fluorescence microscopy images of 20-fs, 100-on-1 damage sites on an RAR silica sample, organized by femtosecond-laser fluence (horizontal) and excitation wavelength of the microscope (vertical). The fluorescence signal was integrated for wavelengths of more than 400 nm.

This change represents a significant increase in transmission loss compared to the pristine RAR metasurface that has transmission loss of less than 0.1%. The lower-fluence morphology (NBOHC defects) did not show any loss of transmission during these measurements with low-power, near-infrared wavelengths. Although a practical analysis may consider one or both of these morphologies to be 'undamaged' based on the transmission results, both will be considered as damaged for the purposes of this work. It has been shown that fatigue is a dose-dependent process[20], and while the work presented here indicates measurable material changes accumulated after only 100 pulses, it is considered that subsequent evolution of the morphology will occur following exposure to the larger number of pulses necessary for short-pulse, high-peak-power laser system operation.

A remaining important consideration is the role of the vacuum environment in the formation of laser-generated surface defects. It has been shown that exposure of silica to near-ultraviolet, nanosecond pulses or near-infrared, femtosecond pulses in a vacuum environment leads to additional formation of defects exhibiting strong photoluminescence accompanied by changes that affect the laser transmission, the scattering of light from the surface and the reduction of the laser-damage threshold[29–32]. These observations are consistent with the aforementioned results of this work.

3.2. LIDT results

The measured LIDT values are plotted in Figure 7(a) on a log–log scale as a function of pulse duration. Extra data points at the 20-fs duration correspond to the two different identified morphologies (generation of ODC or NBOHC defects), as well as repeated multipulse testing of the second sample set that was used for the analysis of damage-site fluorescence and transmission. A significant difference in absolute performance is observed between the two RAR samples, indicating that metasurface damage resistance may be sensitive to manufacturing parameters (such as residual contamination from the reactive-ion-etching process or change in nanotexture element morphology that alters the electric-field enhancement profile), handling, aging or potentially other parameters.

In order to better interpret trends from the data, two additional plots depict comparisons among the data. Figure 7(b) considers the RAR damage performance by taking the ratios of the multipulse LIDT (R-on-1 or 100-on-1) divided by the respective single-pulse LIDT. Therefore, ratios greater than one correspond to laser conditioning, while ratios less than one correspond to fatigue. There is clearly a trend of conditioning with nanosecond duration and fatigue with subpicosecond and femtosecond durations, presumably due to the respective importance of precursor defects versus

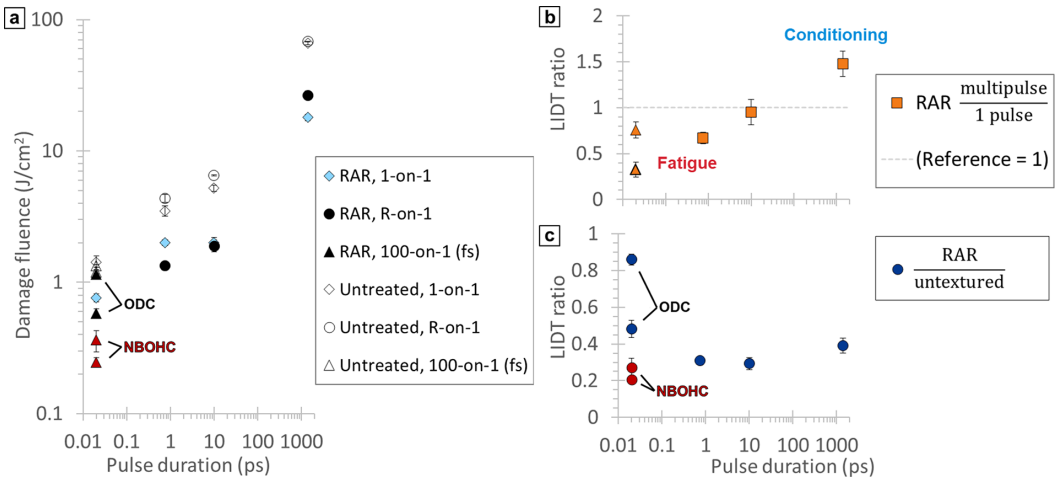

Figure 7. Experimental LIDT results. (a) All measured LIDT values as a function of pulse duration. (b) Ratio of LIDT values from multipulse tests (R-on-1 or 100-on-1) divided by those of single-pulse tests (1-on-1). (c) Ratio of LIDT values of the RAR samples divided by those of the untextured samples. Additional data points for 20-fs duration correspond to an additional sample.

https://doi.org/10.1017/hpl.2025.10036 Published online by Cambridge University Press

localized intensity as the driving factor of damage initiation between the two regimes.

The second comparative plot in Figure 7(c) considers RAR damage performance with respect to the untextured substrates. Specifically, the ratio is taken of the multipulse LIDT values of the RAR samples divided by the respective values for the untextured samples. This analysis indicates that among all pulse durations tested, the damage onset for the RAR metasurface occurred in the range of 20%–40% of the untextured surface LIDT. At pulse duration of 20 fs, NBOHC formation was observed at a fluence level approximately two to three times lower than the onset of ODC formation.

4. Simulation of electric-field distribution

High-spatial-resolution 3D simulations were performed using the finite-difference time-domain method on a 4-μm × 4-μm × 5-μm grid with 10-nm resolution. A 1053-nm plane wave at normal incidence was propagated onto a SiO_2 substrate with a metasurface of 400-nm-tall, super-Gaussian-shaped pillars. To create the metasurface, pillars are inserted with random positions (allowed to overlap) until the average fill ratio is about 50%. This method was used to model an approximation of the actual structure of the metasurface, as observed in SEM images, due to the difficulty in accurately measuring the precise 3D geometry of the nanostructure elements. The 50% fill factor was estimated based on analysis of the SEM cross-sectional images. The resulting simulated transmission value of this structured interface is 99.9%.

Figure 8 shows a visualization of the simulated structure and example values of the numerically simulated electric-field intensity (EFI) distribution inside the pillars and the substrate. The spatial EFI distribution is a complex interference pattern where the EFI at each location results from interactions with many pillars. The results indicate that there are EFI peaks in two general locations: in the lower half of some pillars and in sections of the top few-hundred nanometers of the substrate. In both cases, the distribution is highly speckled, such that only a minority of pillars actually have EFI hot spots, and the hot-spot distribution in the substrate is not laterally uniform. The set of local maximum EFI values in the pillars generally tends to be higher than those in the substrate, but both represent significant increases above the bulk EFI value of 0.69. This bulk value is simply calculated by considering perfect transmission of energy through the surface, but with propagation speed reduced by the refractive index n, yielding $EFI_{bulk} = 1/n$. The maximum EFI value observed in the entire simulation domain was 1.74, which is about 2.5× larger than that of bulk EFI. In the example cross-section of Figure 8(b), a pillar hot spot can be seen reaching about 1.8× bulk EFI, as well as a substrate hot spot reaching about 1.3× bulk EFI.

5. Discussion

The simulation results indicate that localized electric-field intensifications are present in both the nanostructures and just below the nanostructured layer. Such ‘hot spots’ may be responsible for the observed reduction of the LIDT compared to an untextured substrate. In the case of short pulses, the damage would be expected to initiate at locations of the highest EFI (somewhere in the pillars). For longer pulses, one may expect damage to initiate based on a convolution of the EFI distribution and the (unknown) distribution of precursor defects/contamination near the interface of the nanostructured layer with the substrate, where the damage-initiation mechanism is similar (or the same) to that known to prevail in fused-silica (flat) optics under similar excitation conditions.

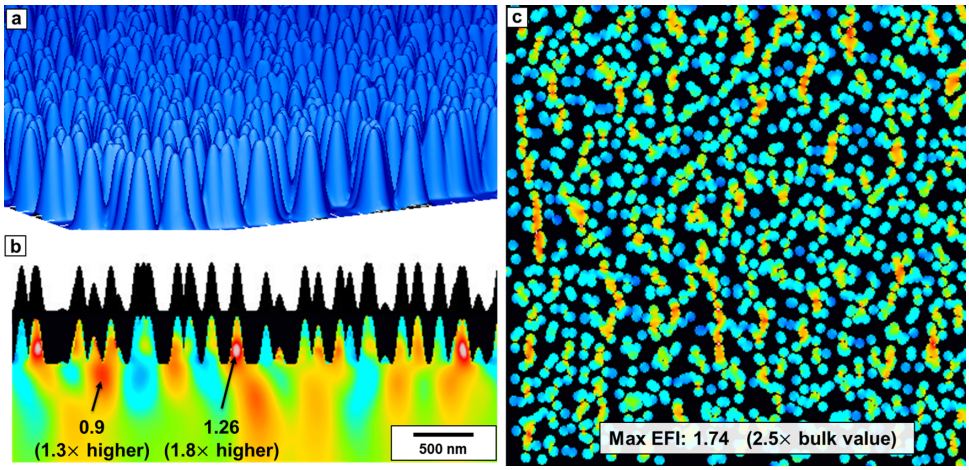

Figure 8. Simulated metasurface shape and example cross-sectional color maps of EFI distribution. (a) Perspective view of the structure. (b) Example side-view cross-section, with the top (black) showing the structure and the bottom (color) mapping the EFI, with laser polarization directed into the page. (c) Example top-view cross-section mapping the EFI at a height in the middle of the nanopillars, with laser polarization oriented vertically. Black indicates the location of air/vacuum.

https://doi.org/10.1017/hpl.2025.10036 Published online by Cambridge University Press

The above reasoning appears to be consistent with the observed damage morphologies. The 0.8-ps damage (as in Figure 4) indicates a superficial ablation of a few neighboring pillars. On the other hand, the morphologies of the 1.4-ns damage sites (as in Figure 2) suggest that the damage typically initiates by forming a (confined) subsurface plasma. The 10-ps pulse duration, showing two types of craters (phenomena observed previously in thin films[16]), may be associated with the initiation of damage in each of the two types of hot-spot locations. Seemingly, the 250-nm-deep, wider craters might be associated with initiation near the bottom of the nanostructures, and the 100-nm-deep, smaller craters might be associated with damage initiation at the location of high EFI in the pillars, similar to the morphologies observed with 0.8-ps duration. The 20-fs damage did not exhibit sufficient material removal, at least to be detectable with our characterization tools, until the fluence was far above threshold, suggesting that the high peak intensity over such a short period of time favors the formation of atomic-scale defects without enough total absorbed energy for appreciable material removal. The mechanism of defect formation is not clear and may be related to nanoscale damage (as discussed in the context of Refs. [22,23]) or via a vacuum-catalyzed photochemical reaction (as discussed in Refs. [25,26]).

Finally, the 2.5× enhancement determined with simulations may be consistent with the overall LIDT reduction of the RAR metasurface to a value in the range of 20%–40% of the untextured substrate LIDT, shown in Figure 7(c). Strictly speaking, this value of 2.5× reduction corresponds to a drop to 40%, and this should only be correlated with damage initiating in pillars. The precise value of peak EFI would also be subject to the exact nanostructure shape and distribution. Furthermore, the correct full picture would also need to consider the fact that the manufacturing process of reactive ion etching can introduce contamination/defects that degrade the LIDT performance independently from EFI considerations[33]. Nonetheless, the observed correlation of the experimental and simulation results suggests that the modeling approximations sufficiently capture the underlying mechanisms. This suggests that the best-possible performance of antireflective metasurfaces may ultimately be limited by the near-field distribution of intensity introduced by the metasurface itself.

In conclusion, the present work has investigated the near-infrared laser-induced damage performance of a fused-silica RAR metasurface design as a function of the pulse duration. The overarching objective was to develop a preliminary understanding of the behavior of silica-based metasurface optics under exposure to short-pulse, high-peak-power laser irradiation to explore failure mechanisms. Owing to the high damage resistance of fused silica, this set of samples may be representative of the performance of high-damage-threshold metasurface optics currently under development for operation over a wide range of pulse durations. Finite-difference time-domain 3D simulations indicated localized electric-field enhancement introduced by the nanostructures, which seems to correlate with the reduction of damage resistance. Morphological analysis revealed that the damage initiations with nanosecond and picosecond pulses caused localized modification and removal of the nanostructures, whereas the damage onset with 20-fs pulses was observed as the creation of electronic defects.

Acknowledgements

The authors acknowledge BAE Systems for funding the acquisition of the initial test samples, and TelAztec for providing additional samples. This material is based upon work supported by the Department of Energy (National Nuclear Security Administration), University of Rochester 'National Inertial Confinement Program' under Award Number(s) DE-NA0004144.

This publication was prepared as an account of work conducted by the Laboratory for Laser Energetics and their sponsors. Neither the sponsors nor any agency thereof, nor any of their employees, makes any warranty, express or implied, or assumes any legal liability or responsibility for the accuracy, completeness or usefulness of any information, apparatus, product or process disclosed, or represents that its use would not infringe privately owned rights. Reference herein to any specific commercial product, process or service by trade name, trademark, manufacturer or otherwise does not necessarily constitute or imply its endorsement, recommendation or favoring by the sponsors or any agency thereof. The views and opinions of the authors expressed herein do not necessarily state or reflect those of the sponsors or any agency thereof.

References

1. W. Cai and V. Shalaev, *Optical Metamaterials: Fundamentals and Applications* (Springer, New York, 2010).
2. M. Liu, W. Zhu, P. Huo, L. Feng, M. Song, C. Zhang, H. J. Lezec, Y. Lu, A. Agrawal, and T. Xu, Light Sci. Appl. **10**, 107 (2021).
3. N. J. Ray, J.-H. Yoo, H. T. Nguyen, M. Norton, D. Cross, C. W. Carr, and E. Feigenbaum, Appl. Opt. **62**, 8219 (2023).
4. H. A. Atikian, N. Sinclair, P. Latawiec, X. Xiong, S. Meesala, S. Gauthier, D. Wintz, J. Randi, D. Bernot, S. DeFrances, J. Thomas, M. Roman, S. Durrant, F. Capasso, and M. Lončar, Nat. Commun. **13**, 2610 (2022).
5. N. Bonod, P. Brianceau, J. Daurios, S. Grosjean, N. Roquin, J.-F. Gleyze, L. Lamaignère, and J. Neauport, Nat. Commun. **14**, 5383 (2023).
6. S. J. Wilson and M. C. Hutley, Opt. Acta: Int. J. Opt. **29**, 993 (1982).
7. D. Hobbs and B. MacLeod, Proc. SPIE **5786**, 349 (2005).
8. M. Modaresialam, N. Granchi, M. Stehlik, C. Petite, S. Delegeanu, A. Gourdin, M. Bouabdellaoui, F. Intonti, B. Kerzabi, D. Grosso, L. Gallais, and M. Abbarchi, Opt. Express **32**, 12967 (2024).

https://doi.org/10.1017/hpl.2025.10036 Published online by Cambridge University Press

9. D. Hobbs, B. MacLeod, and J. Riccobono, Proc. SPIE **6545**, 65450Y (2007).
10. D. Hobbs, B. MacLeod, and E. Sabatino, Proc. SPIE **8530**, 85300O (2012).
11. N. J. Ray, J.-H. Yoo, H. T. Nguyen, and E. Feigenbaum, Adv. Opt. Mater. **10**, 2200151 (2022).
12. A. Papadopoulos, E. Skoulas, A. Mimidis, G. Perrakis, G. Kenanakis, G. D. Tsibidis, and E. Stratakis, Adv. Mater. **31**, 1901123 (2019).
13. E. Skoulas, A. Mimidis, A. Papadopoulos, A. Lemonis, and E. Stratakis, PhotonicsViews **19**, 46 (2022).
14. M. Mende, L. Jensen, H. Ehlers, S. Bruns, M. Vergöhl, P. Burdack, and D. Ristau, Proc. SPIE **8530**, 85300W (2012).
15. A. A. Kozlov, J. C. Lambropoulos, J. B. Oliver, B. N. Hoffman, and S. G. Demos, Sci. Rep. **9**, 607 (2019).
16. R. A. Negres, C. J. Stolz, K. R. P. Kafka, E. A. Chowdhury, M. Kirchner, K. Shea, and M. Daly, Proc. SPIE **10014**, 100140E (2016).
17. T. Z. Kosc, A. A. Kozlov, S. Papernov, K. R. P. Kafka, K. L. Marshall, and S. G. Demos, Sci. Rep. **9**, 16435 (2019).
18. A. A. Kozlov, S. Papernov, J. B. Oliver, A. Rigatti, B. Taylor, B. Charles, and C. Smith, Proc. SPIE **10014**, 100141Y (2017).
19. K. R. P. Kafka, T. Z. Kosc, and S. G. Demos, Opt. Eng. **61**, 071605 (2022).
20. L. Smalakys, B. Momgaudis, R. Grigutis, S. Kičas, and A. Melninkaitis, Opt. Express **27**, 26088 (2019).
21. B. Boizot, S. Agnello, B. Reynard, R. Boscaino, and G. Petite, J. Non-Cryst. Solids **325**, 22 (2003).
22. Mohanty, N. C. Mishra, S. V. Bhat, P. K. Basu, and D. Kanjilal, J. Phys. D **36**, 3151 (2003).
23. S. Nagata, S. Yamamoto, K. Toh, B. Tsuchiya, N. Ohtsu, T. Shikama, and H. Naramoto, J. Nucl. Mater. **329–333**, 1507 (2004).
24. C. D. Marshall, J. A. Speth, and S. A. Payne, J. Non-Cryst. Solids **212**, 59 (1997).
25. F. Messina, L. Vaccaro, and M. Cannas, Phys. Rev. B **81**, 035212 (2010).
26. S. O. Kucheyev and S. G. Demos, Appl. Phys. Lett. **82**, 3230 (2003).
27. A. Zoubir, C. Rivero, R. Grodsky, K. Richardson, M. Richardson, T. Cardinal, and M. Couzi, Phys. Rev. B **73**, 224117 (2006).
28. V. De Michele, E. Marin, A. Boukenter, M. Cannas, S. Girard, and Y. Ouerdane, Phys. Status Solidi A **218**, 2000802 (2021).
29. S. G. Demos, A. Burnham, P. Wegner, M. Norton, L. Zeller, M. Runkel, M. R. Kozlowski, M. Staggs, and H. B. Radousky, Electron. Lett. **36**, 566 (2000).
30. A. K. Burnham, M. J. Runkel, S. G. Demos, M. R. Kozlowski, and P. J. Wegner, Proc. SPIE **4134**, 243 (2000).
31. D. N. Nguyen, L. A. Emmert, P. Schwoebel, D. Patel, C. S. Menoni, M. Shinn, and W. Rudolph, Opt. Express **19**, 5690 (2011).
32. S.-Z. Xu, H.-B. Lv, X.-D. Yuan, J. Huang, X.-D. Jiang, H.-J. Wang, X.-T. Zu, and W.-G. Zheng, Chin. Phys. Lett. **25**, 223 (2008).
33. R. Dent, A. L. Rigatti, A. A. Kozlov, S. G. Demos, and A. Shestopalov, "Investigation of inductively coupled plasma reactive ion etching for multilayer dielectric grating fabrication," submitted to Optics Express (2025).

https://doi.org/10.1017/hpl.2025.10036 Published online by Cambridge University Press